Solar Energy Materials & Solar Cells 292 (2025) 113804

Contents lists available at ScienceDirect

Solar Energy Materials and Solar Cells

journal homepage: www.elsevier.com/locate/solmat

Radiator tailoring for enhanced performance in InAs-based Near-field thermophotovoltaics

Mathieu Giroux [a,*], Sean Molesky [b], Raphael St-Gelais [a,c,d], Jacob J. Krich [c,d]

[a] Department of Mechanical Engineering, University of Ottawa, Ottawa K1N 6N5, Ontario, Canada
[b] Department of Engineering Physics, Polytechnique Montreal, Montreal H3T 1J4, Quebec, Canada
[c] Department of Physics, University of Ottawa, Ottawa K1N 6N5, Ontario, Canada
[d] Nexus for Quantum Technologies, University of Ottawa, Ottawa K1N 6N5, Ontario, Canada

ARTICLE INFO

Keywords:
InAs
Near-field thermophotovoltaics
Dielectric model
Free carrier absorption
Drude model

ABSTRACT

Near-field thermophotovoltaics (NFTPV) systems have significant potential for waste heat recovery applications, with both high theoretical efficiency and power density, up to 40% and 11 W/cm^2 at 900 K. Yet experimental demonstrations have only achieved up to 14% efficiency and modest power densities (i.e., 0.75 W/cm^2). While experiments have recently started to focus on photovoltaic (PV) cells custom-made for NFTPV, many studies still rely on doped silicon radiators. In this work, we design an optimized NFTPV radiator for an indium arsenide-based system and, in the process, investigate models for the permittivity of InAs in the context of NFTPV. Based on existing measurements of InAs absorption, we find that the traditional Drude model overestimates free carrier absorption in InAs. We replace the Drude portion of the InAs dielectric function with a revised model derived from ionized impurity scattering. Using this revised model, we maximize the spectral efficiency and power density of a NFTPV system by optimizing the spectral coupling between a radiator and an InAs PV cell. We find that when the radiator and the PV cell are both made of InAs, a nearly threefold improvement of spectral efficiency is possible compared to a silicon radiator with the same InAs cell. This enhancement reduces subgap thermal transfer while maintaining power output.

1. Introduction

Waste heat above 600 K represents 10% of the global energy consumption [1]. Harvesting this energy would significantly enhance energy-use efficiency and reduce carbon emissions. For 600–900 K heat sources, thermoelectric generators (TEGs) are the most-widely used solid-state technology [2]. While TEGs have experimentally achieved high power densities up to 22 W/cm^2 at 868 K [3], conduction losses limit achievable efficiencies [4], which are typically less than 10% [2]. Thermophotovoltaic (TPV) systems present an alternative, potentially efficient, solid-state solution, with theoretical efficiencies up to 45% at 900 K [2], but are limited to low power densities, below 0.2 W/cm^2 at 900 K [2]. Near-field thermophotovoltaics (NFTPV) systems have significant potential for waste heat recovery applications [5–9], with both high theoretical efficiency and power density, up to 40% and 11 W/cm^2 at 900 K [6]. This technology exploits the drastic enhancement of the thermal radiation between two bodies at subwavelength distances due to evanescent radiative thermal coupling. When a cold photovoltaic (PV) cell is positioned in such close proximity to a hot radiator, tremendous amounts of heat transfer from the hot object to the PV cell, where it can be converted to electricity.

Despite such potential, experimental demonstrations have only achieved up to 14% efficiency and 0.75 W/cm^2 power density [10–13]. One of the main challenges in the development of NFTPV technology is the need for specialized narrow-bandgap PV cells. Early demonstrations [10,11] relied on basic PV cells fabricated in house [11] or on commercially available photodetectors [10]. The use of PV cells unoptimized for near-field operations resulted in modest performance, with conversion efficiencies below 1% and less than 1 nW of generated power. Recently, PV cells optimized for NFTPV operation [12,13] were reported, leading to higher efficiencies and power densities, up to 14% and 0.75 W/cm^2, which are still far from the predicted limits [5–9].

One reason for the gap between high theoretical performances and modest experimental results is that many experimental studies still rely on doped Si radiators [10,13,14]. A few theoretical works reported optimized radiator designs for NFTPV applications [8,9]. These studies relied on plasmonic materials, such as indium-tin-oxide (ITO), which exhibit surface polariton resonances in the infrared region, enhancing the radiative heat flux in a spectral distribution located just above the bandgap of the PV cell. While these materials greatly improve the

* Corresponding author.
E-mail address: mgiro027@uottawa.ca (M. Giroux).

https://doi.org/10.1016/j.solmat.2025.113804
Received 13 December 2024; Received in revised form 4 June 2025; Accepted 20 June 2025
Available online 4 July 2025

theoretical performance of NFTPV systems, in practice their optical properties are contingent upon factors such as film annealing and deposition conditions [15], making the experimental implementation of these proposed films quite challenging. Here, with eye towards near-term large-scale implementation, we focus on the more practical and reproducible possibilities offered by crystalline materials.

For the temperature range of waste heat recovery applications (< 1000 K [10]), InAs is a promising material [6,16,17], with a bandgap (0.35 eV) well aligned to the Planck spectrum. To predict the properties of InAs in a NFTPV system, an accurate dielectric model is imperative to correctly model the radiative heat transfer spectrum. For this purpose, most dielectric models employ a Drude form for the free-carrier absorption.

We have found that this choice leads to a consistent overestimation of free carrier absorption, both above and below the bandgap, especially for highly doped InAs. Here, we correct this overestimation by substituting the Drude response for a revised model, derived from ionized impurity scattering [18], and, using this refinement, design an optimized radiator for an InAs-based NFTPV system.

We compare the performance of a doped silicon radiator to that of a doped InAs radiator, both paired with an InAs-based photovoltaic cell designed specifically for NFTPV [16]. We find that, when the doping levels and thicknesses of the radiators are chosen optimally, the power output from both radiators is nearly identical, but the spectral efficiency is higher with an InAs radiator. Namely the use of a silicon radiator leads to increased subgap heat transfer, due to an additional subgap resonance. In addition to improving the heat transfer spectrum, reducing such subgap heat transfer lowers cooling requirements and is therefore highly desirable.

2. Results and discussion

2.1. Dielectric function

Calculating radiative heat transfer requires knowledge of the dielectric functions of all materials used (in our case Si and InAs) from low energy up to several times the material bandgap. For Si, we use a dielectric model containing lattice and interband contributions from Ref. [19] combined with the Drude free-carrier model from Ref. [20], while incorporating the mobility, decay rates and donor and acceptor contributions from Ref. [21]. All of these models have been validated against experimental data in Refs. [19,20], and [21]. For InAs, we employ the comprehensive dielectric model assembled in Ref. [22] with the updated parameters from Ref. [16]. This dielectric model includes a Drude–Lorentz model to account for both lattice and free carrier contributions, as well as an interband absorption model with non-parabolicity corrections and the Moss–Burstein shift. Non-parabolicity corrections are employed as both the valence and conduction bands deviate significantly from a simple quadratic relationship at the energies relevant to this study. The Moss–Burstein shift is included to account for band filling effects, which are significant in InAs due to both its small bandgap and its light effective mass, leading to a shift in the effective bandgap. Note that, unlike Ref. [22], we employ an approximation to the Kramers–Kronig relations to improve computational speed, following the approach of Ref. [16] (see Appendix for full discussion). A Python implementation and a detailed description of these dielectric models can be found in Ref. [23].

Based on existing measurements of InAs absorption [24–26], we find that the traditional Drude model, proposed for example in Ref. [22], overestimates free carrier absorption in InAs. Fig. 1(a) compares the InAs absorption coefficient from the dielectric model described in Ref. [22] to experimental n-doped InAs absorption data at different donor concentrations N_d taken from Refs. [24,25], and [26]. The comparison suggests that the Drude contribution results in a significant overestimation of free carrier absorption at energies near the bandgap. This discrepancy becomes more noticeable at higher doping

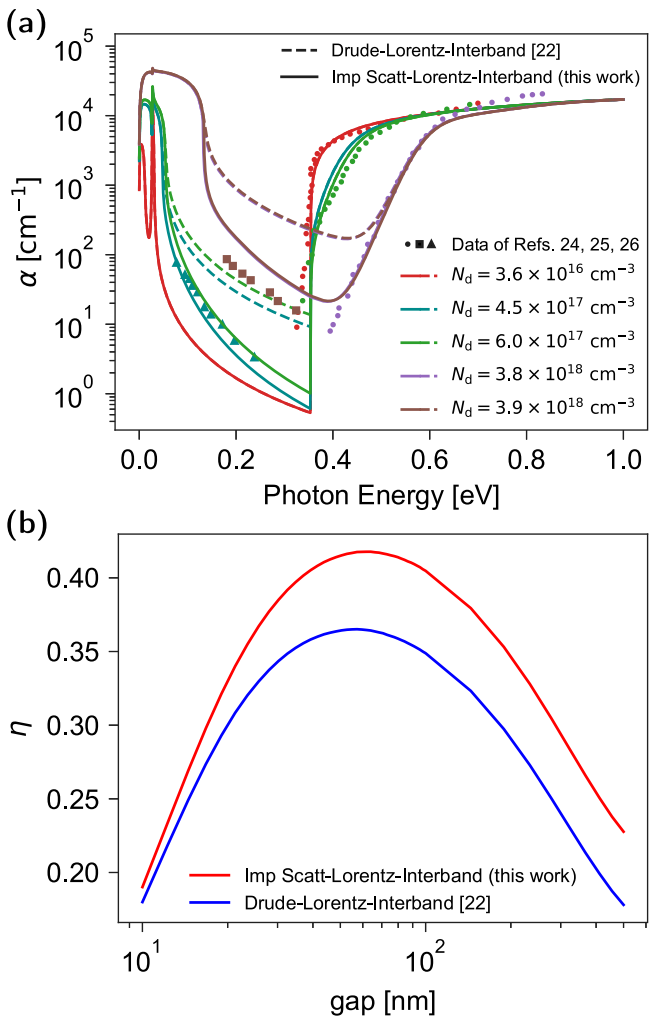

Fig. 1. (a) InAs absorption coefficient from the dielectric model of Ref. [22] (dashed lines), which combines a Drude–Lorentz model with an interband model (Drude–Lorentz-Interband), compared to data from n-doped InAs (markers). Our revised model, which replaces the Drude model with an ionized impurity scattering model (Imp Scatt-Lorentz-Interband), significantly improves the agreement with experimental data above and below the bandgap, especially at high doping. Circles from Ref. [24], squares from Ref. [25], and triangles from Ref. [26]. (b) Computed spectral efficiency, with the Drude–Lorentz-Interband model (blue) and with our proposed model (red), as a function of the gap for an InAs-based NFTPV system using an InAs radiator. The Drude model underestimates the spectral efficiency by up to 22% because it overestimates below-bandgap free carrier absorption.

levels, leading to an overestimation of absorption above the bandgap. These differences cause inaccurate model predictions of NFTPV performances as above-bandgap absorption originating from free carrier absorption does not generate collectible electron–hole pairs. Additionally, parasitic subgap heating has a considerable effect on the overall performance of the device.

We address this overestimation by incorporating an alternative model, described in Ref. [18], derived from screened ionized impurity scattering. The discrepancies in Fig. 1(a) are most significant at high doping concentration, which is precisely where ionized impurity scattering is strongest. The Drude model is widely used for its simplicity, and it is able to accurately and generically describe the low-frequency dielectric function—and thus free-carrier absorption—in many semiconductors. There are many physically motivated dielectric models that could be used in place of the Drude model, including those considering acoustic phonons and plasmon effects [18]. Models accounting for optical phonons were not considered here, as this effect

is already captured by the Lorentz model. We select a model based on screened ionized impurity scattering because it provides a physically motivated form that agrees with the Drude model at low frequency but produces an absorption coefficient that decays more rapidly at higher frequency. It is also computationally tractable. While adjusting the loss parameter in the Drude model may appear to be the most straightforward approach to address this issue, we find that reducing this parameter decreases high-frequency absorption but compromises the accuracy in the low-frequency region. The corrective model is only valid when the Fermi level E_F measured from the conduction band minimum is larger than the thermal energy and the frequency ω exceeds the plasma frequency ω_p, given by

$$\omega_p = \sqrt{\frac{Ne^2}{\varepsilon_0 \varepsilon_\infty m_e^*}}, \tag{1}$$

where N is the carrier density, e is the elementary charge, ε_0 is the vacuum permittivity, ε_∞ is the high-frequency dielectric constant, and m_e^* is the electron conduction band effective mass. Therefore, we still employ the Drude model when $\omega < \omega_p$ or when E_F is below the thermal energy. For highly n-doped InAs, when $\omega > \omega_p$, the corrective model substitutes the imaginary component of the Drude model ε''_{FC} with

$$\varepsilon''_{FC}(\omega) = A\zeta^{-4}\int_{(1-\zeta)\theta(1-\zeta)}^{1}\left[\frac{1}{2}\ln\frac{\left(\sqrt{X+\zeta}+\sqrt{X}\right)^2+X_{TF}}{\left(\sqrt{X+\zeta}-\sqrt{X}\right)^2+X_{TF}} - \frac{2X_{TF}\sqrt{X(X+\zeta)}}{\left[\left(\sqrt{X+\zeta}+\sqrt{X}\right)^2+X_{TF}\right]\left[\left(\sqrt{X+\zeta}-\sqrt{X}\right)^2+X_{TF}\right]}\right]dX \tag{2}$$

where $\zeta = \frac{\hbar\omega}{E_F}$, $X_{TF} = \left(\frac{q_{TF}}{k_F}\right)^2$, $q_{TF} = \sqrt{\frac{3Ne^2}{2\varepsilon_0\varepsilon_\infty E_F}}$ is the Thomas–Fermi screening wavevector, $A = \frac{1}{12\pi^3}\frac{e^2\gamma k_F^4}{\varepsilon_0 E_F^3}$, $k_F = \frac{\sqrt{2m_e^* E_F}}{\hbar}$ is the Fermi wavevector, $\gamma = R\left[\frac{Ze^2}{\varepsilon_0\varepsilon_\infty k_F^2}\right]^2$, and $\theta(x)$ is the Heaviside step function. Here, $\hbar$ is the reduced Planck constant, Z is the charge number of the impurity, and R denotes the number of impurities with charge $Z \cdot e$. Eq. (2) was derived assuming statically screened matrix elements for the interaction of electrons with ionized impurities. This static approximation of the dynamical screening of charges by conduction electrons breaks down at lower frequencies (i.e., $\omega < \omega_p$), which is why the model is only valid for $\omega > \omega_p$ [18]. With this new form for $\varepsilon''_{FC}(\omega)$, we can use the Kramers–Kronig relations to find the corresponding modification to the real part of the dielectric $\varepsilon'_{FC}(\omega)$. We have confirmed that simply using ε'_{FC} from the original Drude model introduces less than 1% error in ε'_{FC} in a highly doped test case. Note that in Eq. (1), N is set to the doping concentration. For an InAs radiator with a doping level of $2\times10^{18}\,\mathrm{cm^{-3}}$ at 1000 K, accounting for thermally generated carriers results in a carrier concentration of $3.57\times10^{18}\,\mathrm{cm^{-3}}$. However, we find that neglecting the contribution of thermally excited carriers only results in a 0.025% overestimation of P and a 0.37% underestimation of η. The contribution of thermally excited carriers would become significant at lower doping concentrations and should be included in such cases. Our freely available implementation of the model, available in Ref. [23], includes an option to account for this contribution.

The proposed model more adequately represents the free carrier contribution and results in a good agreement with the experimental data at doping levels below $10^{18}\,\mathrm{cm^{-3}}$ (see Fig. 1). While this is a significant improvement, the model could be further refined as we continue to observe approximately a twofold overestimation of the free carrier contribution at high doping levels (e.g., $N_d = 3.8\times10^{18}\,\mathrm{cm^{-3}}$ near 0.4 eV).

In Fig. 1(b), we compare the spectral efficiency of a NFTPV system using an optimized InAs radiator computed with a Drude model to that computed with our proposed model; details on the optimization and calculation of spectral efficiency are in the next section. We find that the standard Drude model results in up to a 22% underestimation of the spectral efficiency due to the overestimation of below bandgap absorption.

2.2. Radiator optimization

2.2.1. InAs as a radiator

Using a one-dimensional fluctuational electrodynamics model from Ref. [27], which employs a frequency-domain Maxwell-equation solver, we attempt to improve NFTPV system performance via optimization of radiator material. Our goal is to determine whether an InAs radiator outperforms a doped Si radiator in an InAs-based NFTPV system. We consider an InAs PV cell designed specifically for high efficiency NFTPV [16], which was designed assuming a silicon radiator, and compare the performance of a NFTPV system using a silicon or InAs radiator. The PV device modeled in this work consists of a p-i-n-n^+ InAs structure, depicted in Fig. 2, with the n^+ layer effectively forming a reflector for subgap radiation. The layers in this p-i-n-n^+ structure are designated as the front surface field (FSF), emitter, base, and back reflector (BR), respectively. Note that the high doping level in the BR layer is achievable experimentally [28]. This high doping level leads to $\omega_p > E_g$. As described in Section 2.1, the ionized impurity model is employed only for $\omega > \omega_p$, so the BR layer uses the Drude model and thus has an overestimation of absorptivity. In all simulations, the PV cell is assumed to operate at 300 K. We assess the performance of NFTPV systems using two key metrics: the useful transferred power P and the spectral efficiency η [9],

$$P = \int_{\frac{E_g}{\hbar}}^{\infty}\frac{E_g}{\hbar\omega}Q(\omega)\mathrm{d}\omega, \tag{3}$$

$$\eta = \frac{P}{\int_0^\infty Q(\omega)\mathrm{d}\omega}, \tag{4}$$

where E_g is the bandgap energy and $Q(\omega)$ is the spectral heat flux. P is an upper limit to useful power, where we assume that all energy transfer with $\omega > E_g/\hbar$ generates electron–hole pairs, and that they each give E_g of useful energy, also known as the Trivich-Flinn efficiency limit [29]. Note that the figures of merit presented in Eqs. (3) and (4) are not associated with a real diode, as the losses through electroluminescence—accounted for in the Shockley–Queisser model [30]—are not included. The spectral efficiency considers the inefficiencies from above-gap heat transfer, where the PV cell cannot use all of the energy, as well as subgap heat transfers that do not produce electron–hole pairs but still heat the PV cell.

The radiative heat flux absorbed by the PV device depends on several factors, including the radiator doping level and thickness, gap, and temperature. Therefore, prior to comparing the performance of the two radiator materials, we must optimize the radiator parameters for various fixed gaps and temperatures.

2.2.2. Optimization of the radiator parameters

Before comparing radiator materials, we must first select appropriate thicknesses and doping levels. To ensure a fair comparison, we optimize these parameters for each radiator material. We choose four representative test conditions (700 and 1000 K radiator temperatures with 30 and 100 nm gaps) and optimize the radiator thickness and doping level at each test condition. Our goal is to select a radiator design that can perform well at a variety of temperatures and gaps. We first identify optimal designs for each test condition, and then select the design with the best average performance across the four test conditions.

We consider both finite and semi-infinite thickness radiators separately. We analyze the performance of semi-infinite thickness radiators to study the behavior of bulk materials. We simulate semi-infinite thickness radiators by generating an output medium behind the radiator

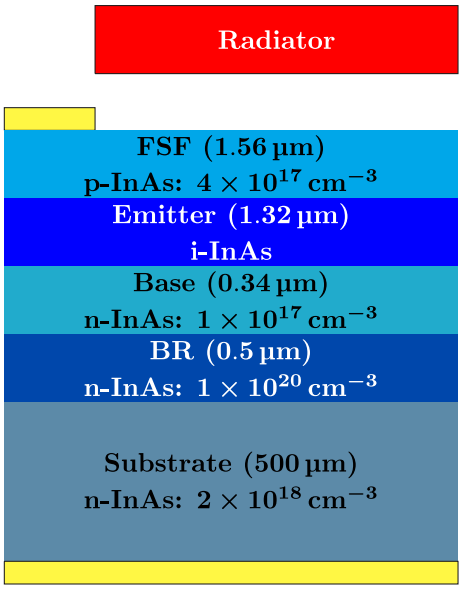

Fig. 2. Illustration of the InAs-based NFTPV system for which we design an optimized radiator.

made of the same material, neglecting any transmission through the layer. This semi-infinite medium removes any spurious Fabry–Pérot interference effect that can arise in the case of a finite stack. Radiators can effectively behave as semi-infinite at achievable thicknesses as low as 100 µm depending on the material and doping level, and this approach enables us to compute the performance of such bulk radiators much faster than if we considered large finite-thickness radiators.

We optimize for the quantity $P \cdot \eta$ since we want large power densities with high efficiency. Optimizing either P or η on its own does not capture these effects. Although optimizing P is essential, it is equally important to optimize η, as poor spectral efficiency leads to significant parasitic subgap radiation, heating the cell and increasing cooling requirements. We explored independent optimizations of P and η, but found that the optimization of one parameter often results in a significant reduction in the other. For instance, in the case of finite-thickness InAs, optimizing for P alone—compared to optimizing for $P \cdot \eta$—yields a 4.1% increase in P at the expense of more than a fivefold decrease in η.

Our optimizer relies on the Nelder–Mead method implemented in the Optim package in Julia. Initial guesses are generated using a coarse 5×5 grid for the doping level and radiator thickness. After finding optimal finite and semi-infinite designs for each material under each test condition, we normalize the $P \cdot \eta$ value by dividing it by its maximum across all radiator designs for each test condition. We then compute the average normalized $P \cdot \eta$ value across all test conditions and select the design with the largest average. The selected optimal finite and semi-infinite designs are reported in Table 1. In Table 1, we note that, for Si, a semi-infinite thickness radiator offers better performance, while for InAs, a finite thickness radiator is more effective. It is worth mentioning that in Table 1, the doping levels for the Bulk and Thin Si radiators differ significantly, as thinner radiators need higher carrier concentrations to be optically thick above 0.35 eV. While semi-infinite radiators can behave as optically thick at low doping levels, finite-thickness radiators require higher doping levels to ensure sufficient free-carrier absorption above the InAs bandgap.

2.2.3. InAs vs Si

We first compare, in Fig. 3, the performance of the two semi-infinite radiators, one InAs and the other Si, for which the doping level was optimized (Bulk InAs and Bulk Si designs). In the case of a semi-infinite radiator, InAs achieves significantly higher spectral efficiency,

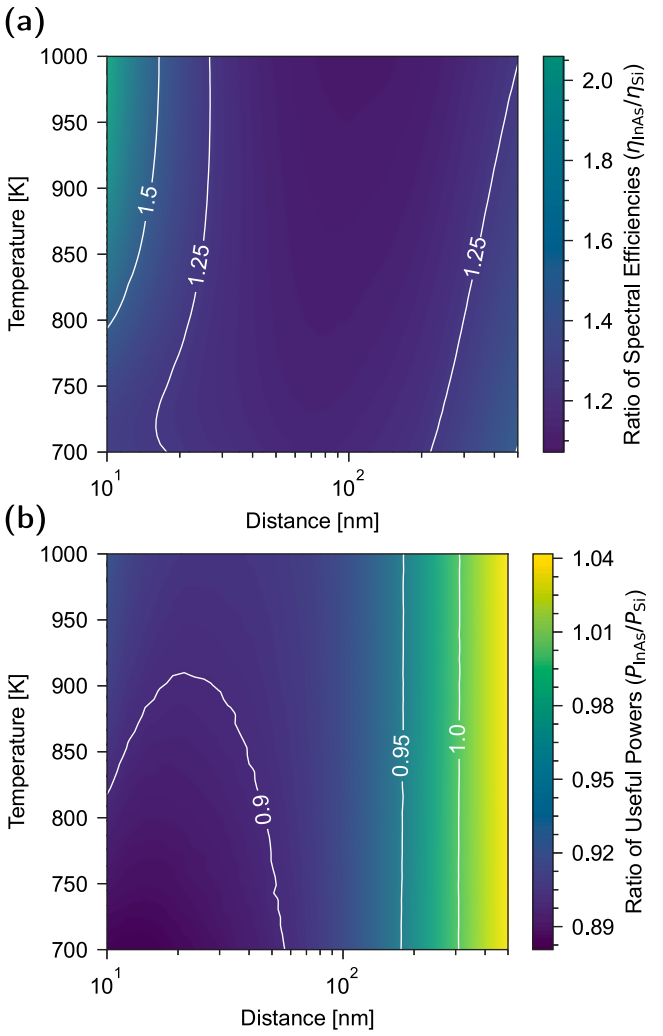

Fig. 3. Bulk InAs vs Bulk Si: (a) Spectral efficiency ratio and (b) useful power ratio. For bulk radiators, InAs offers greater spectral efficiency at the expense of a relative reduction in useful power of over 11% at small gaps.

particularly at small gaps and elevated temperatures. InAs, however, suffers from more than 11% relative reduction in useful power at small gaps.

In Table 1, we note that, for Si, a semi-infinite radiator offers the best performance, while for an InAs radiator, a finite-thickness radiator is more effective. In fact, the Finite InAs radiator improves the average $P \cdot \eta$ by approximately 5%. We, therefore, compare these two best cases (Finite InAs design vs Bulk Si design) in Fig. 4. The Finite InAs radiator significantly improves spectral efficiency at larger gaps, while offering a useful power similar to that of a silicon radiator. Conversely, at smaller gaps, the thinner InAs radiator achieves greater useful power than the semi-infinite and is at most only 7% lower than the Si radiator, though this power comes with a small reduction in the spectral efficiency.

Since experimental NFTPV platforms often rely on thin films, we compare, in Fig. 5, the performance of the two radiator materials using finite-thickness designs (< 100 µm). In this case, an InAs radiator significantly improves the spectral efficiency, achieving nearly a threefold enhancement at small distances, while only resulting in a reduction in useful power of at most 5%.

2.2.4. Underlying phenomena

To study the origin of the spectral efficiency enhancement observed with an InAs radiator, Fig. 6 compares the spectral heat flux of both

Table 1
Optimized finite and semi-infinite NFTPV radiator designs with their performance at each test condition.

Radiator Design	Radiator Material	Thickness [μm]	Doping [cm^{-3}]	$P \cdot \eta$ [$kW\,cm^{-2}$]			
				700 K		1000 K	
				30 nm	100 nm	30 nm	100 nm
Bulk InAs	n-doped InAs	∞	4.6×10^{18}	4.89	3.13	68.5	42.7
Finite InAs	n-doped InAs	6.5	2×10^{18}	5.15	3.56	68.8	43.6
Bulk Si	p-doped Si	∞	1×10^{17}	4.51	2.92	62.1	43.3
Finite Si	p-doped Si	100	1×10^{20}	2.94	2.45	52.4	40.3

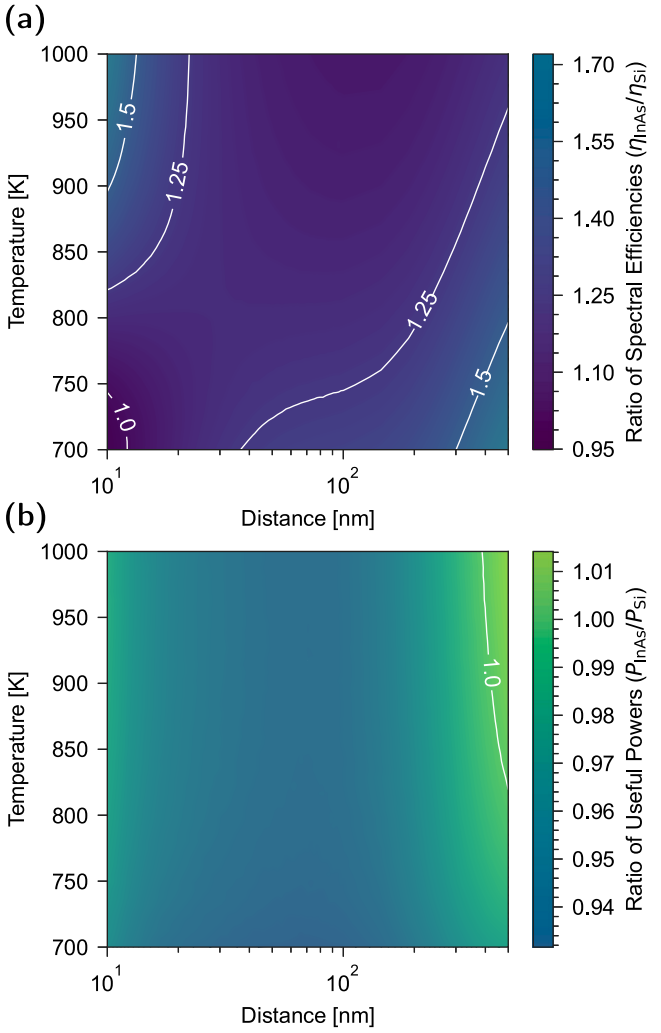

Fig. 4. Best-case InAs vs best-case Si, i.e., Finite InAs vs Bulk Si: (a) Spectral efficiency ratio and (b) useful power ratio. An InAs radiator offers greater spectral efficiency and comparable useful power.

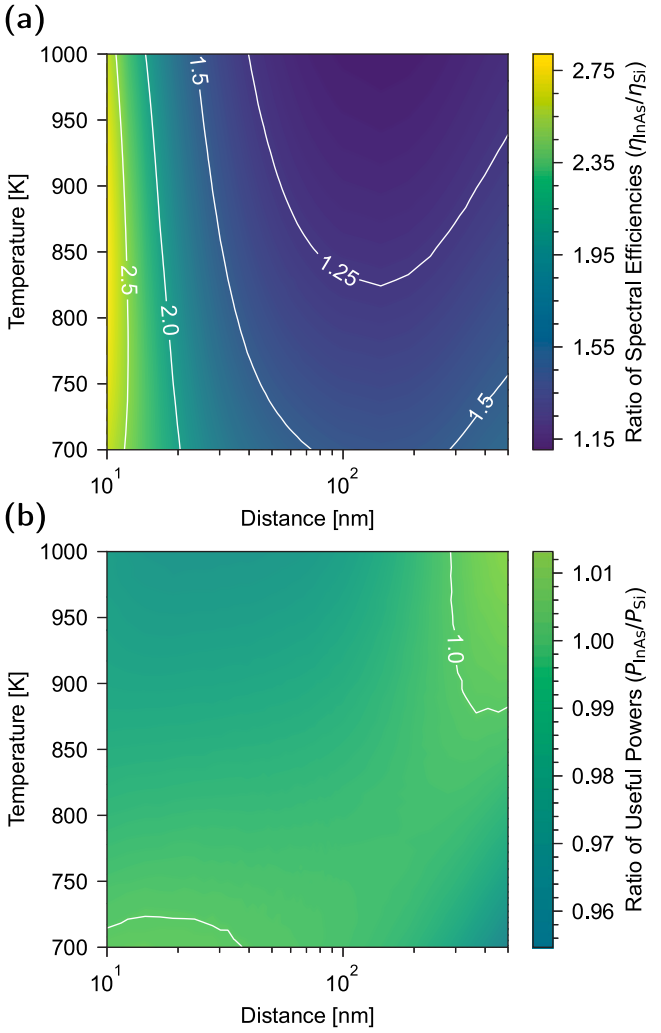

Fig. 5. Finite InAs vs Finite Si: (a) Spectral efficiency ratio and (b) useful power ratio. For thin-film radiators, InAs offers greater spectral efficiency, achieving nearly a threefold enhancement at small distances, with a reduction in useful power of at most 5%.

radiator materials. Compared to the Si radiator, subgap heat absorption is substantially reduced with the InAs radiator, without significantly affecting the above-bandgap heat absorption. This reduction is further illustrated in Fig. 7, which shows the spatially resolved spectral absorption in the PV cell, accounting for the contributions from both evanescent and propagating modes. A comparison of Figs. 7(a) and 7(b) reveals that the InAs radiator significantly reduces the below-bandgap absorption in the n^+ layer that acts as a back reflector. Although a reduction in the front-surface p-region is not immediately apparent in Fig. 7, the InAs radiator results in a 53% reduction of below-bandgap absorption in this layer. While index matching generally leads to enhanced heat flux, this is not the effect observed in Fig. 6. Since the optical constants of InAs vary with temperature, the large temperature difference between the radiator and PV cell prevents the InAs radiator from benefiting from index matching. For example, the bandgap (0.354 eV at 300 K vs. 0.246 eV at 700 K) varies significantly with temperature, so the radiator and PV cell have distinct optical properties, even if they are made of the same material.

To study how the optical properties of InAs results in such improvement, Fig. 8 contrasts the absorption coefficient of the FSF to the InAs radiator (i.e., doping of the Finite InAs design), and the Si radiator (i.e., doping of the Finite Si design). This comparison shows that the absorption coefficient of InAs is much lower than that of Si at energies just below the bandgap. According to the Kirchhoff law, under isothermal conditions, the emissivity of a material is proportional to its absorption coefficient. Therefore, the absorption coefficient of the

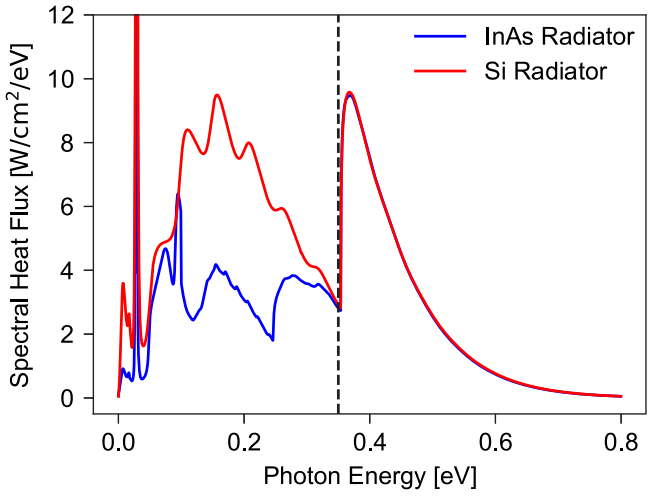

Fig. 6. Spectral radiative heat transfer in an InAs-based NFTPV system using an InAs radiator (Finite InAs design, blue) and a Si radiator (Finite Si design, red) at 700 K and a separation of 100 nm.

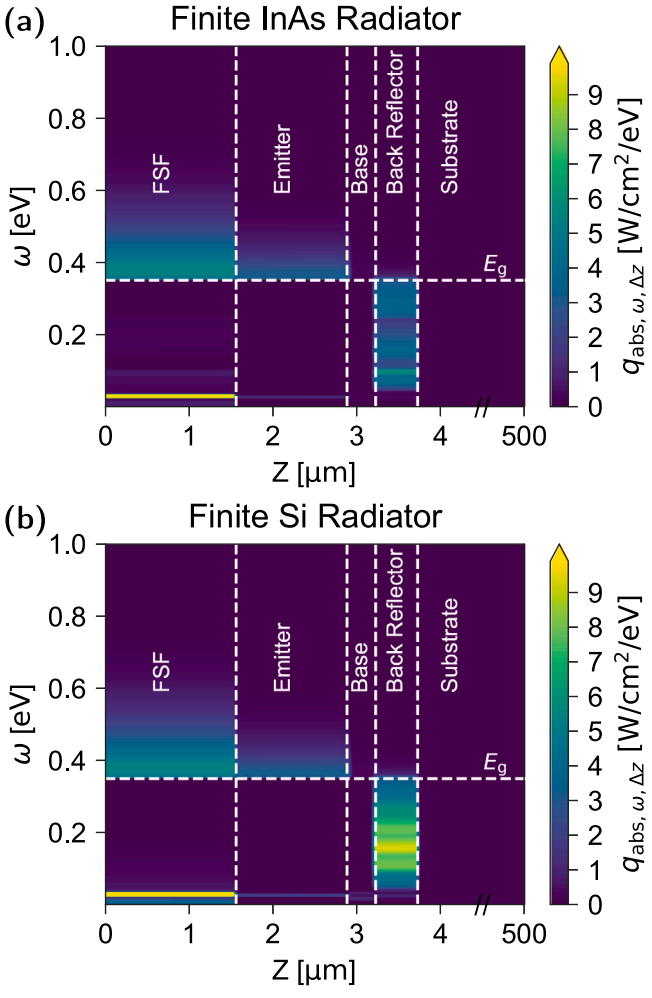

Fig. 7. Spectral–spatial absorption distribution, $q_{abs,\omega,\Delta z}$, within the InAs cell for a separation of 100 nm and a radiator temperature of 700 K using (a) an InAs radiator (Finite InAs design) and (b) a Si radiator (Finite Si design).

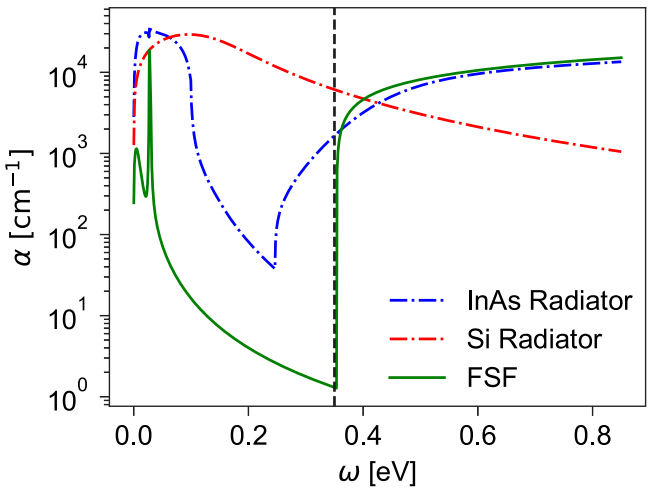

Fig. 8. Absorption coefficient of the FSF layer of the InAs PV cell at 300 K (green), compared with the absorption coefficient of an InAs radiator (Finite InAs design, blue) and a Si radiator (Finite Si design, red), both at 700 K.

radiator plays a crucial role in determining the radiative heat flux. In this case, the lower subgap absorption coefficient of the InAs radiator could explain the reduction in subgap absorption in the BR layer.

We attribute the substantial below-bandgap absorption observed with the Si radiator to a surface polariton resonance. As shown in Fig. 9, for both radiator materials, at a 10 nm separation, the above-bandgap heat transfer is primarily influenced by frustrated modes occurring at a parallel wavevector k_ρ exceeding the vacuum wavevector k_0 but lower than the material light lines (given by $\mathrm{Re}(n)k_0$ where n is the refractive index of the material) [31]. These results also demonstrate that, for Si, the below-bandgap radiative heat flux is dominated by a resonance at $\omega = 0.0255\,\mathrm{eV}$. This resonance originates from surface polariton resonances in the Si radiator, since its parallel wavevector exceeds both material light lines. This below-bandgap surface resonance is anticipated since silicon has a plasma resonance below bandgap ($\omega_p = 0.198\,\mathrm{eV}$ for the Finite Si design [21]). Conversely, InAs is a polar material with a resonance around 0.028 eV, which is slightly noticeable in Fig. 9(a). However, this resonance is much narrower than the plasmonic resonance in Si, leading to less below-bandgap emission. Consequently, the presence of a slowly decaying below-bandgap surface polariton resonance in Si explains why an InAs radiator significantly enhances spectral efficiency.

3. Conclusions

We have demonstrated that the spectral efficiency of NFTPV systems can be greatly enhanced when both the PV cell and radiator are made of InAs. In such a case, spectral coupling results in a significant improvement in spectral efficiency compared to a doped Si radiator, achieving nearly a threefold enhancement at small distances. This improvement reduces the parasitic heating of the PV cell and increases its overall efficiency while not significantly affecting the power density. Additionally, utilizing InAs for both the PV cell and the radiator could be advantageous for monolithic fabrication in a single crystal growth process for both the radiator and the PV cell. During our analysis, we also uncovered an overestimation of free carrier absorption in InAs dielectric function models. We implement a corrective model and demonstrate that it accurately represents the absorption at moderate doping levels but could be further refined for improved accuracy at higher doping levels.

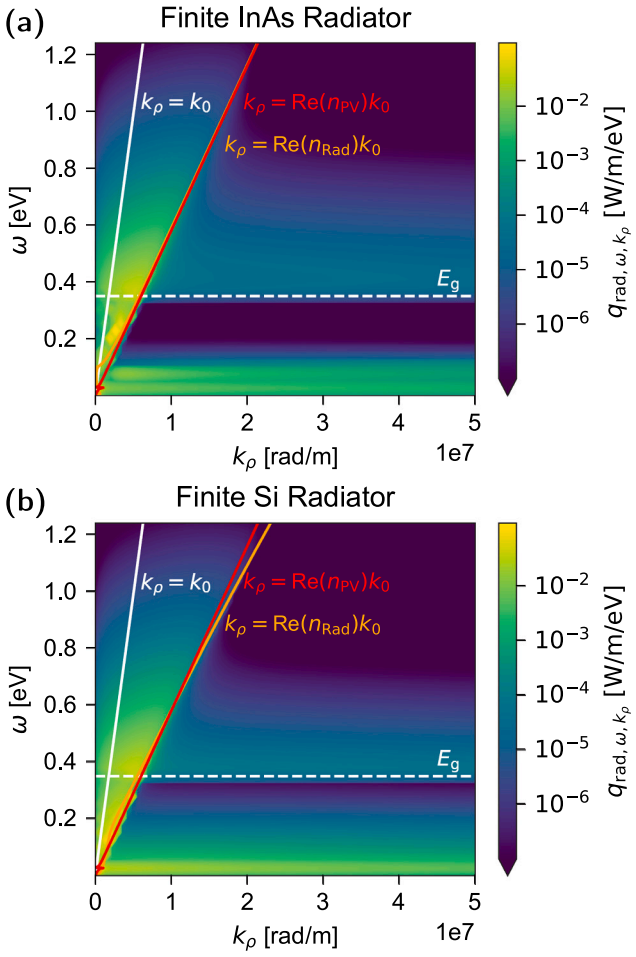

Fig. 9. Radiative heat flux, $q_{\mathrm{rad},\omega,k_\rho}$, per unit angular frequency, ω, and parallel wavevector, k_ρ, at a 10 nm separation and a radiator temperature of 700 K for (a) an InAs radiator (Finite InAs design) and (b) a Si radiator (Finite Si design). For both materials, the above-bandgap radiative heat flux is primarily influenced by frustrated modes ($k_0 < k_\rho < k_0 \min\left(\mathrm{Re}(n_{\mathrm{Rad}}), \mathrm{Re}(n_{\mathrm{PV}})\right)$), while propagating modes ($k_\rho < k_0$) have modest contributions. For Si, the below-bandgap radiative heat flux is significantly dominated by surface polariton resonances ($k_\rho > k_0 \min\left(\mathrm{Re}(n_{\mathrm{Rad}}), \mathrm{Re}(n_{\mathrm{PV}})\right)$).

CRediT authorship contribution statement

Mathieu Giroux: Writing – review & editing, Writing – original draft, Software, Methodology, Investigation, Conceptualization. **Sean Molesky:** Writing – review & editing, Software, Methodology. **Raphael St-Gelais:** Writing – review & editing, Funding acquisition, Conceptualization. **Jacob J. Krich:** Writing – review & editing, Supervision, Methodology, Investigation, Funding acquisition, Conceptualization.

Declaration of competing interest

The authors declare that they have no known competing financial interests or personal relationships that could have appeared to influence the work reported in this paper.

Acknowledgments

The authors thank Mathieu Francoeur from the University of Utah and Daniel Milovich from the Universidad Politécnica de Madrid for useful discussions on the dielectric model of InAs. The authors also thank Mauro Antezza from the Institut Universitaire de France for stimulating discussions on the Kramers–Kronig relations. The authors also extend their gratitude to University of Ottawa colleague Gavin Forcade for discussions on permittivity and heat transfer calculation algorithms. This work was funded by the Natural Sciences and Engineering Research Council of Canada (NSERC) through the CREATE TOP-SET program (No. 497981) and the CGS-D program.

Appendix. Kramers–Kronig relations in InAs dielectric model

In Ref. [22], the real part of the interband refractive index n'_{IB} is calculated from the imaginary part of the interband refractive index n''_{IB}, using the Kramers–Kronig relations. Similarly, the contribution from Eq. (2) to the real part of the permittivity ε', can be determined using the Kramers–Kronig relations. Unfortunately, the Kramers–Kronig relations can be computationally expensive. Therefore, to avoid a Kramers–Kronig calculation, we instead approximate $n'_{\mathrm{IB}} = \sqrt{\varepsilon_\infty}$, following the approach of Ref. [16], and employ the Drude model to describe the real part of the permittivity due to free carrier absorption. We find that this approximation results in an underestimation of both the useful transferred power and the spectral efficiency of approximately 1% and 4%, relative, respectively.

Note that NFTPV simulations only require optical constants up to approximately 1.5 eV, although the Kramers–Kronig relations involve integration over the entire frequency range. In our dielectric model, the interband absorption model, taken from Ref. [32], is based on $k \cdot p$ theory and is therefore only valid near the absorption edge. In this case, the light-hole absorption contribution obeys $\alpha_{\mathrm{lh}}(\omega) \sim \omega$ as $\omega \to \infty$, leading to a non-convergent Kramers–Kronig relation. This limit is not physical, and the α_{lh} term can be smoothly suppressed at energies above 1 eV with only a few percent change in the Kramers–Kronig derived interband refractive index n'_{IB} depending on the exact form of the suppression function. We consider such changes to be within the expected errors for the modeled optical constants. Also note that we evaluate the interband absorption coefficient α_{IB} by considering only the contributions from the light-hole and heavy-hole bands, as the contributions from remote bands are accounted for in ε_∞. Absorption from the split-off hole band begins at approximately 0.75 eV, and above this energy, α_{IB} is already underestimated.

Data availability

InAs and silicon dielectric model descriptions and Python implementations are available in Ref. [23]. Data for figures is available on request.

References

[1] C. Forman, I.K. Muritala, R. Pardemann, B. Meyer, Estimating the global waste heat potential, Renew. Sustain. Energy Rev. 57 (2016) 1568–1579.
[2] I.A.O. Tedah, F. Maculewicz, D.E. Wolf, R. Schmechel, Thermoelectrics versus thermophotovoltaics: two approaches to convert heat fluxes into electricity, J. Phys. D: Appl. Phys. 52 (27) (2019) 275501.
[3] R. He, D. Kraemer, J. Mao, L. Zeng, Q. Jie, Y. Lan, C. Li, J. Shuai, H.S. Kim, Y. Liu, D. Broido, C.-W. Chu, G. Chen, Z. Ren, Achieving high power factor and output power density in p-type half-Heuslers Nb 1-x Ti x FeSb, Proc. Natl. Acad. Sci. 113 (48) (2016) 13576–13581.
[4] A. Datas, R. Vaillon, Thermionic-enhanced near-field thermophotovoltaics, Nano Energy 61 (2019) 10–17.
[5] M. Laroche, R. Carminati, J.-J. Greffet, Near-field thermophotovoltaic energy conversion, J. Appl. Phys. 100 (6) (2006) 063704.
[6] B. Zhao, K. Chen, S. Buddhiraju, G. Bhatt, M. Lipson, S. Fan, High-performance near-field thermophotovoltaics for waste heat recovery, Nano Energy 41 (2017) 344–350.
[7] S. Molesky, Z. Jacob, Ideal near-field thermophotovoltaic cells, Phys. Rev. B 91 (2015) 205435.
[8] O. Ilic, M. Jablan, J.D. Joannopoulos, I. Celanovic, M. Soljačić, Overcoming the black body limit in plasmonic and graphene near-field thermophotovoltaic systems, Opt. Express 20 (S3) (2012) A366–A384.
[9] R. St-Gelais, G.R. Bhatt, L. Zhu, S. Fan, M. Lipson, Hot carrier-based near-field thermophotovoltaic energy conversion, ACS Nano 11 (3) (2017) 3001–3009.

[10] A. Fiorino, L. Zhu, D. Thompson, R. Mittapally, P. Reddy, E. Meyhofer, Nanogap near-field thermophotovoltaics, Nature Nanotechnology 13 (9) (2018) 806—811.
[11] G.R. Bhatt, B. Zhao, S. Roberts, I. Datta, A. Mohanty, T. Lin, J.-M. Hartmann, R. St-Gelais, S. Fan, M. Lipson, Integrated near-field thermo-photovoltaics for heat recycling, Nat. Commun. 11 (1) (2020) 2545.
[12] C. Lucchesi, D. Cakiroglu, J.-P. Perez, T. Taliercio, E. Tournié, P.-O. Chapuis, R. Vaillon, Near-field thermophotovoltaic conversion with high electrical power density and cell efficiency above 14%, Nano Lett. 21 (11) (2021) 4524–4529.
[13] R. Mittapally, B. Lee, L. Zhu, A. Reihani, J.W. Lim, D. Fan, S.R. Forrest, P. Reddy, E. Meyhofer, Near-field thermophotovoltaics for efficient heat to electricity conversion at high power density, Nat. Commun. 12 (1) (2021) 4364.
[14] T. Inoue, T. Koyama, D.D. Kang, K. Ikeda, T. Asano, S. Noda, One-chip near-field thermophotovoltaic device integrating a thin-film thermal emitter and photovoltaic cell, Nano Lett. 19 (6) (2019) 3948–3952.
[15] M. Alam, D. Cameron, Investigation of annealing effects on sol–gel deposited indium tin oxide thin films in different atmospheres, Thin Solid Films 420–421 (2002) 76–82, Proceedings of the 29th International Conference on Metallurgic Coatings and Thin Films.
[16] G.P. Forcade, C.E. Valdivia, S. Molesky, S. Lu, A.W. Rodriguez, J.J. Krich, R. St-Gelais, K. Hinzer, Efficiency-optimized near-field thermophotovoltaics using InAs and InAsSbP, Appl. Phys. Lett. 121 (19) (2022) 193903.
[17] J. Selvidge, R.M. France, J. Goldsmith, P. Solanki, M.A. Steiner, E.J. Tervo, Large area near-field thermophotovoltaics for low temperature applications, 2024, arXiv preprint arXiv:2408.01295.
[18] R. von Baltz, W. Escher, Quantum theory of free carrier absorption, Phys. Status Solidi (b) 51 (2) (1972) 499–507.
[19] B.J. Lee, Z.M. Zhang, E.A. Early, D.P. DeWitt, B.K. Tsai, Modeling radiative properties of silicon with coatings and comparison with reflectance measurements, J. Thermophys. Heat Transfer 19 (4) (2005) 558–565.
[20] C. Fu, Z. Zhang, Nanoscale radiation heat transfer for silicon at different doping levels, Int. J. Heat Mass Transfer 49 (9) (2006) 1703–1718.
[21] S. Basu, B.J. Lee, Z.M. Zhang, Infrared radiative properties of heavily doped silicon at room temperature, J. Heat Transf. 132 (2) (2009) 023301.
[22] D. Milovich, J. Villa, E. Antolin, A. Datas, A. Marti, R. Vaillon, M. Francoeur, Design of an indium arsenide cell for near-field thermophotovoltaic devices, J. Photonics Energy 10 (2) (2020) 025503–025503.
[23] M. Giroux, MatGiroux/Permittivity: Initial Release, Zenodo, 2025.
[24] J.R. Dixon, J.M. Ellis, Optical properties of n-type indium arsenide in the fundamental absorption edge region, Phys. Rev. 123 (5) (1961) 1560.
[25] J.R. Dixon, Optical absorption mechanisms in indium arsenide, in: Proceedings of 5th International Conference on Physics of Semiconductors, Prague, 1960, p. 366.
[26] R.M. Culpepper, J.R. Dixon, Free-carrier absorption in n-type indium arsenide, JOSA 58 (1) (1968) 96–102.
[27] S. Molesky, heatSlabs, 2020, https://github.com/SeanMolesky/HeatSlabs.
[28] A. Baraskar, V. Jain, M.A. Wistey, U. Singisetti, Y.J. Lee, B. Thibeault, A. Gossard, M.J.W. Rodwell, High doping effects on in-situ ohmic contacts to n-inas, in: 2010 22nd International Conference on Indium Phosphide and Related Materials, IPRM, 2010, pp. 1–4.
[29] M.A. Green, Analytical treatment of Trivich–Flinn and Shockley–Queisser photovoltaic efficiency limits using polylogarithms, Prog. Photovolt., Res. Appl. 20 (2) (2012) 127–134.
[30] W. Shockley, H.J. Queisser, Detailed balance limit of efficiency of p-n junction solar cells, J. Appl. Phys. 32 (3) (1961) 510–519.
[31] J. DeSutter, L. Tang, M. Francoeur, A near-field radiative heat transfer device, Nature Nanotechnology 14 (8) (2019) 751–755.
[32] W. Anderson, Absorption constant of Pb1-xSnxTe and Hg1-xCdxTe alloys, Infrared Phys. 20 (6) (1980) 363–372.